Received: 26 March 2020 | Revised: 22 May 2020 | Accepted: 14 June 2020

DOI: 10.1111/jace.17339

ORIGINAL ARTICLE

Journal of the American Ceramic Society

CeO_2 and CeO_2:Pr nanocrystalline powders prepared by the polymeric precursor method: Yellow and red pigments with tunable color

Luiziana Aparecida Gonzaga[1] | **Vinicius Tadeu Santana**[2] | **Maria Inês Basso Bernardi**[3] | **Jakub Hrubý**[2] | **Petr Neugebauer**[2] | **Alexandre Mesquita**[1]

[1]Institute of Geosciences and Exact Sciences, São Paulo State University (Unesp), Rio Claro - SP, Brazil

[2]CEITEC – Central European Institute of Technology, Brno University of Technology, Brno, Czech Republic

[3]São Carlos Institute of Physics, University of São Paulo - USP, São Carlos - SP, Brazil

Correspondence
Alexandre Mesquita, Institute of Geosciences and Exact Sciences, São Paulo State University (Unesp), Rio Claro - SP, Brazil.
Email: alexandre.mesquita@unesp.br

Funding information
Fundação de Amparo à Pesquisa do Estado de São Paulo, Grant/Award Number: 2013/12993-4; Conselho Nacional de Desenvolvimento Científico e Tecnológico; CEITEC Nano Research Infrastructure, Grant/Award Number: MEYS CR (LM2018110); Ministry of Education, Youth and Sports of the Czech Republic, Grant/Award Number: CEITEC 2020 (LQ1601); Coordenação de Aperfeiçoamento de Pessoal de Nível Superior

Abstract

The development of stable and reproducible inorganic pigments is noteworthy for industrial applications mainly considering more intense shades and low toxicity. Among the various candidates to substitute non-hazardous red and yellow pigments, CeO_2 and CeO_2:Pr have been attracting attention because of their opacity and high-temperature stability besides being environmental-friendly and health-friendly. In this study, nanostructured CeO_2 and CeO_2:Pr samples were synthesized using the polymeric precursor method and structural and optical characterizations were performed. Scanning electron microscopy reveals the morphology of CeO_2 nanoparticles in which the particle size ranges from 22 to 28 nm as a function of the annealing temperature. Pr-doping does not show influence on the particle size. XRD results show that CeO_2 and CeO_2:Pr samples crystallize in the cubic fluorite lattice with *Fm3m* space group. Raman spectra show the fluorite F_{2g} mode, confirming the XRD results. With Pr-doping and the annealing of the samples, two bands are observed between 550 and 600 cm^{-1}, which are related to the defects in the fluorite structure associated with oxygen vacancies. XPS spectra reveal an increase in the ratio of Ce^{3+} ions depending on the annealing temperature and Pr-doping. This increase is associated with the carbon removal from the lattice by annealing. This behavior causes a change in the hue of the powders as the annealing temperature increases. According to diffuse reflectance and colorimetric measurements, CeO_2 shows a light-yellow color due to the O 2pCe 4f transitions whose b* parameter mainly decreases with annealing, becoming almost white. The CeO_2:Pr sample exhibits a red-orange color because of the electronic transitions between $4f^2 \rightarrow 5d^1$ states of Pr^{3+}. Upon annealing, L* and b* parameters decrease, resulting in a red-brown shade. The charge compensation or charge transfer is responsible for the modification of the hue of these pigments.

KEYWORDS
cerium/cerium compounds, nanostructures, pigment, rare earths

1 | INTRODUCTION

Inorganic pigments are extensively used in several fabrication processes in the industry because of their high thermal and chemical resistance, durability, and hiding power by comparison to organic pigments.[1] However, many inorganic pigments contain toxic elements such as Hg, Cd, Se, Sb, Pb, Co, and Cr, which are hazardous to health and environment.[2–4] Environmental and health problems concern all the ceramic pigments, however, the use of the toxic chromophores Cd, Pb, or Cr is emphasized in red and yellow conventional ceramic pigments.[2,5]

In this sense, there is currently great interest in the development of inorganic pigments with thermal and chemical stability, more intense shades and low toxicity. Among the various candidates to substitute non-hazardous red and yellow pigments, ceria (CeO_2) and its associated materials are very relevant because of opacity and high-temperature stability besides to be environmental-friendly and health-friendly.[2–5] The CeO_2 allows the formation of extended solid solutions with a diversity of atoms incorporated into the cubic fluorite-like lattice with space group *Fm*3*m*.[3,6,7] Typically, because of the O 2p-Ce 4f transitions, CeO_2 shows a strong absorption below 400 nm and almost no visible absorption is observed.[4] This compound has been reported as the matrix of the Pr^{3+}or Pr^{4+}chromophores (CeO_2:Pr), resulting in shades that vary from magenta-orange to red-brown, depending on the Pr content, method of preparation and annealing.[3,4,7–11] The most common oxidation state of the praseodymium is 3+ due to the fact that the first three ionization energies are relatively low, as for the other lanthanides.[1,2] As a consequence, there are strong absorptions in the blue and red regions because of the transitions between $4f^2 \rightarrow 5d^1$ states of Pr^{3+}.[1,2] An intensive pink-orange color with the acceptable low content of praseodymium was attributed to the pigment containing 10 mol% of praseodymium.[8,12] When 50 mol% of praseodymium is used, the color hue of the pigment is shifted to red-brown hue. Higher content of praseodymium increases the values of the L* and a* parameters and shifts color to brown–yellow.[8,12] Some studies reported that $Ce_{0.950}Pr_{0.050}O_{2-\delta}$ composition presents the good red color after firing at high temperatures[8,12] whereas Masó et al[11] demonstrated that $Ce_{0.990}Pr_{0.010}O_{2-\delta}$ and $Ce_{0.975}Pr_{0.025}O_{2-\delta}$ compositions prepared by solid-state reaction present the best red colors whose color hue is becoming stronger as calcination temperature increases. Concerning crystal effects, the cell parameter a of CeO_2 fluorite structure decreases with the increasing of the praseodymium content.[8,11,12] Praseodymium atoms substitute cerium atoms in their crystal lattice forming defects, which are related to the decrease of the volume of the elementary cell of CeO_2 due to smaller radius of Pr ions compared to Ce ions.[8] Vacancies due to heterovalent substitution (Pr^{3+} ions in the place of Ce^{4+} ions) are also a type of lattice defects.[8,11,12]

Different methods have been used in order to synthesize CeO_2 particles such as hydrothermal or solvothermal method,[6,13] microwave-assisted hydrothermal,[14] microemulsion,[15,16] impregnation,[17] coprecipitation,[18–20] combustion,[21] and sol-gel.[22,23] As a type of sol-gel preparation, the polymeric precursor method consists of the formation of a polymeric resin from the polymerization of a polyhydroxy alcohol (for example, ethylene glycol) and an α-hydroxycarboxylic acid (for example, citric acid). Before the polymerization, a stable metal complex is formed through the chelation between metal cations and the α-hydroxycarboxylic acid.[24,25] Doping at the molecular level in solution, compositional homogeneity, reduced segregation of metal ions, and low toxicity are examples of the advantages related to this method.[24–28] Doped or pure nanoparticles of CeO_2 have been successfully synthesized through this procedure.[29,30] As this method uses a polymeric resin as a precursor, it has been reported that some materials could contain carbon atoms even after the pyrolysis procedure, creating defects in the lattice, such as interstitial or substitutional carbons.[31,32] The increasing of the annealing temperature causes the initial cleavage of cation-O bonds, resulting in the removal of the O atoms along with C atoms.[31,32] Concerning nanostructured CeO_2 samples, the loss of oxygen at the surfaces of the nanoparticles causes typically the formation of nonstoichiometric compounds of the type $CeO_{2-\delta}$.[6] As a consequence of the introduced oxygen vacancies, a reduction of the Ce^{4+} ions to Ce^{3+} occurs.[6] This reduction has been reported along with the release of oxygen and the modification of the color pigment.[4]

Thus, we aimed to synthesize nanostructured CeO_2 and CeO_2:Pr samples by the polymeric precursor method and to describe the coloring mechanism of these pigments due to this type of preparation. Herein, the structure of these samples was characterized by X-ray diffraction (XRD), field emission scanning electron microscopy (FE-SEM), Raman spectroscopy, X-ray photoelectron spectroscopy (XPS). UV-visible (UV/Vis) diffuse reflectance spectroscopy and colorimetric study were also performed.

2 | EXPERIMENTAL PROCEDURE

$Ce_{1-x}Pr_xO_2$ samples were prepared by the polymeric precursor method with x = 0.00 (CeO_2) and x = 0.01 (CeO_2:Pr). Citric acid, $C_6H_8O_7$ (99.5%, Synth), cerium nitrate hexahydrate, $CeN_3O_9{\cdot}6H_2O$ (99%, Vetec), praseodymium oxide (Pr_2O_3, Alfa Aesar, 99.9%), and ethylene glycol, $C_2H_6O_2$ (99.5%, Synth) were used as precursors according to their stoichiometric amounts. $CeN_3O_9{\cdot}6H_2O$ was dissolved in a citric acid aqueous solution under constant stirring to form cerium citrate. The molar ratio between citric acid and metal

was 3:1. For Pr incorporation, Pr_2O_3 was diluted in a nitric acid solution and then added to the citric acid solution. The polyesterification reaction was promoted by the addition of the $C_2H_6O_2$ in this solution in which the mass ratio between citric acid and ethylene glycol was 60/40. Heat treatment with temperature of 400°C during 4 hours was performed in order to eliminate the organic byproducts due to the polymeric network formation. As-prepared samples were labeled as CeO_2-400 and CeO_2:Pr-400. Then, these samples were annealed at 500, 600, 700, and 800°C for 2 hours. Pr-undoped and Pr-doped samples were labeled as CeO_2-*x* and CeO_2:Pr-*x*, respectively, where *x* signifies the annealing temperature in Celsius degrees.

A RigakuUltima 4 powder diffractometer with geometry θ-2θ was used to perform the XRD measurements at room temperature. This equipment operates with a rotating anode X-ray source with Cu-K_α radiation ($\lambda = 1.542$ Å). The step size and the count time were 0.02° and 5 seconds per step, respectively, during the measurements. Scanning electron microscopy images were acquired using a high-resolution scanning electron microscope Zeiss Sigma. MonoVista CRS Raman spectrometer from S&I were used in order to perform Raman spectra of the samples at room temperature. This spectrometer operates with an Olympus microscope and a He-Ne laser (633 nm line) with 35 mW. Kratos Axis Supra spectrometer was used at room temperature and ultra-high vacuum conditions to record XPS spectra. The instrument was equipped with monochromatic Al Kα source 1486.6 eV (15 mA, 15 kV), and hemispherical analyzer with hybrid magnetic and electrostatic lens for enhanced electron collection. The inelastic backgrounds in all spectra were treated according to Shirley method.[33] Cary 5G spectrophotometer were used in order to collect UV–visible diffuse reflectance spectra in the 200-800 nm range. A spectrophotometer Minolta CM2600d was used to acquire colorimetric coordinates of the samples. The measurements were performed in the 400-700 nm range with standard type D65 (daylight) light source, following the CIE-L*a*b* colorimetric method recommended by the CIE (Commission Internationale de l'Eclairage).[34]

3 | RESULTS AND DISCUSSION

Figure 1 shows the XRD patterns collected at room temperature for CeO_2-400, CeO_2-800, and CeO_2:Pr-400 samples. The samples crystallized without the presence of spurious phases. XRD patterns present broad peaks typical of nanostructures.[35] The peaks are indexed according to the diffraction planes of the fluorite structure with space group *Fm3m* (ICSD no. 156250), in agreement with the literature.[6] The XRD patterns for the CeO_2:Pr composition also do not exhibit secondary phases. In CeO_2 matrix, Pr atoms can substitute Ce atoms because their ionic radii are similar. The ionic radii of $Pr^{3+}$and $Pr^{4+}$are 1.13 and 0.99 Å, respectively, whereas the ionic radii of $Ce^{3+}$and $Ce^{4+}$are 1.15 and 1.01 Å, respectively.[36] The average crystallite size values of samples were calculated using Scherrer's Equation [37] and the full width at half maximum of (111) peaks from the XRD patterns for all samples depicted in Figure 1. The average crystallite size values are equal to 7.9, 7.1, and 12.8 nm for CeO_2-400, CeO_2:Pr-400, and CeO_2-800 samples, respectively. The small decrease observed in the average crystallite size with the Pr incorporation could be associated with the difference between Pr and Ce ionic radii. In this case, hosted Pr ions with smaller size will replace Ce ions in the lattice, resulting in smaller cell parameters since the structure remains the same. Moreover the diffraction peaks become narrower as the annealing temperature increases, indicating a higher degree of crystallinity for this sample. Average crystallite size increases because of the coalescence process of the crystallites as a function of the annealing.

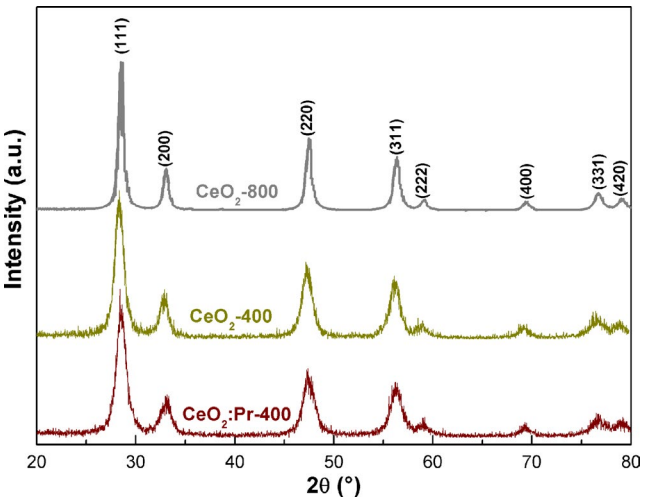

FIGURE 1 XRD patterns for CeO_2-400, CeO_2:Pr-400 and CeO_2-800 samples [Color figure can be viewed at wileyonlinelibrary.com]

The morphology of the CeO_2 and CeO_2:Pr samples prepared by the polymeric precursor method was analyzed using FE-SEM measurements. Figure 2 shows the FE-SEM images for as-prepared CeO_2 powders (CeO_2-400), CeO_2 and CeO_2:Pr powders annealed at 800°C (CeO_2-800 and CeO_2:Pr-800, respectively). Uniform particle size for each sample can be seen in these images and the particle size distribution was evaluated, whose results acquired for the samples are shown in Figure 2D. The average particle size for CeO_2-400, CeO_2-800, and CeO_2:Pr-800 are 22 ± 1, 28 ± 1, and 24 ± 2 nm, respectively. As can be observed, annealing temperature or Pr-doping do not influence significantly on growth rate. The average crystallite size values are smaller than the average particle size evaluated through the FE-SEM measurements, meaning that each particle consists of some coherent diffracting domains, which is in agreement with previous studies.[19,35,38]

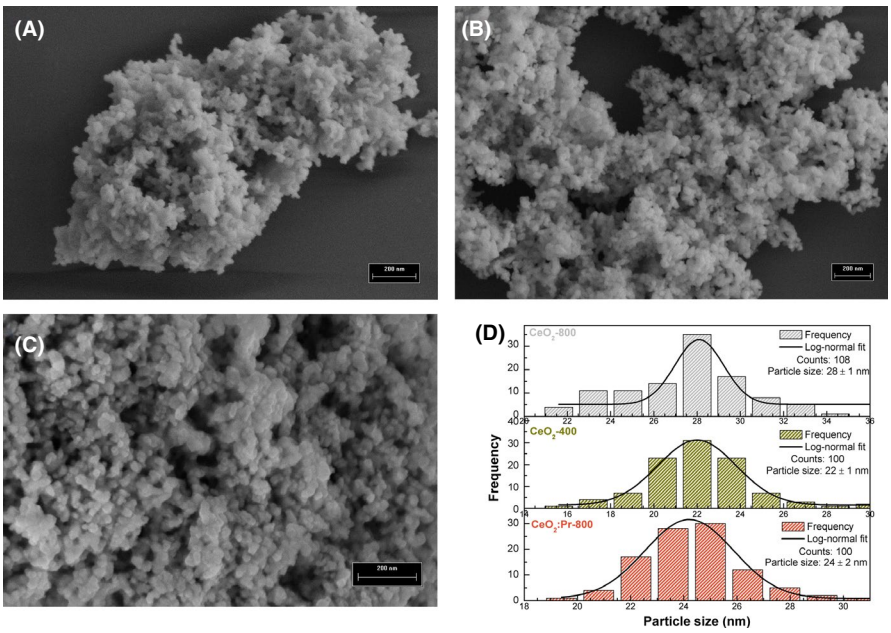

FIGURE 2 FE-SEM images for (A) CeO_2-400, (B) CeO_2-800, and (C) CeO_2:Pr-800 nanostructured samples. (D) Particle size distribution [Color figure can be viewed at wileyonlinelibrary.com]

Figure 3 shows the Raman spectra for CeO_2-400, CeO_2:Pr-400, CeO_2-800, and CeO_2:Pr-800 samples. The main feature centered at 460 $cm^{-1}$is observed in all Raman spectra presented. This peak is associated with the fluorite F_{2g} symmetry mode (symmetric breathing mode of the oxygen atoms around each cation), in agreement with the XRD results.[6,39] Only one Raman mode is allowed in dioxides with a fluorite structure and its frequency is 465 cm^{-1} in bulk CeO_2.[6,39] As the annealing temperature increases, it is possible to observe a shift to higher frequencies, and the peak narrows. This behavior is associated with the increase of the crystallinity degree with the annealing. Moreover a shift to lower frequencies is observed with the Pr-doping, which can be ascribed to defects in the lattice caused by the difference between the ionic radius of host and dopant cations and the formation of oxygen vacancies.[6,39] For CeO_2:Pr samples, a broad band from 550 to 610 cm^{-1} can be observed. This band can be deconvoluted into two other bands. The first one, centered at 550 cm^{-1} has been ascribed to oxygen vacancies because of the charge neutrality due to the substitution of Ce^{4+} ions by Pr^{3+} ions.[6] The band centered at 600 cm^{-1} band is associated with the intrinsic oxygen vacancies caused by the Ce^{3+} ions in the ceria matrix.[6] The intensity of this feature increases as the annealing temperature increases for CeO_2:Pr compound, which can also indicate the increase in oxygen vacancies related to the Pr incorporation into the $CeO_{2-\delta}$ matrix.

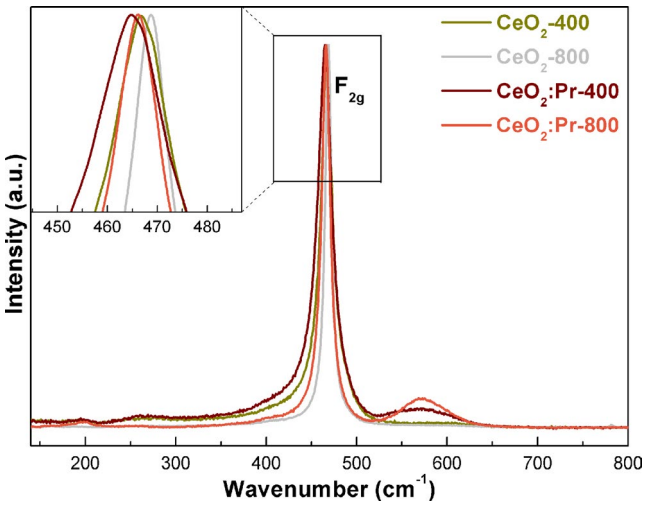

FIGURE 3 Raman spectra for CeO_2-400, CeO_2:Pr-400, CeO_2-800 and CeO_2:Pr-800 samples. The upper left inset indicates the position and width of the peak which is assigned to the fluorite F_{2g} mode [Color figure can be viewed at wileyonlinelibrary.com]

XPS measurements are shown in Figure 4, where Ce^{3+} or Ce^{4+} components are composed by 10 distinct peaks which were fitted in Ce 3d photoemission spectra (Figure 4A).[40] This Figure illustrates that Ce 3d spectrum is formed by 5 peaks for $3d_{3/2}$ (assigned as u°, u, u', u", u"') and other 5 peaks for $3d_{5/2}$ (assigned as v°, v, v', v", v"').[40] In this sense, u"'–v"', u"–v" and u–v are spin–orbit doublets that are associated with different final states of Ce^{4+} after photoexcitation.[40] The u"'–v"' doublet is correlated to Ce^{4+} $3d^94f^0O2p^6$state, the u"–v" doublet to Ce^{4+} $3d^94f^1O2p^5$ and the u–v doublet to Ce^{4+} $3d^94f^2O2p^4$.[40] Similarly, u'–v' and u°–v° spin-orbit doublets are associated with the final states of Ce^{3+} $3d^94f^2O2p^5$ and $Ce^{3+}3d^94f^1O2p^6$, respectively.[40] All the Ce $3d_{3/2}$ and Ce $3d_{5/2}$ XPS spectra indicate majority of cerium as Ce^{4+} oxidation state. An estimation of the percent composition of Ce^{3+} can be calculated using the Equation (1)[41]:

$$\%Ce^{3+} = \frac{A(u') + A(u^0)}{A(u) + A(u') + A(u') + A(u'') + A(u^0)}, \quad (1)$$

where $A(u^n)$ denotes the area of each (n) Ce $3d_{3/2}$ components obtained with the fitting of XPS spectra. This ratio was

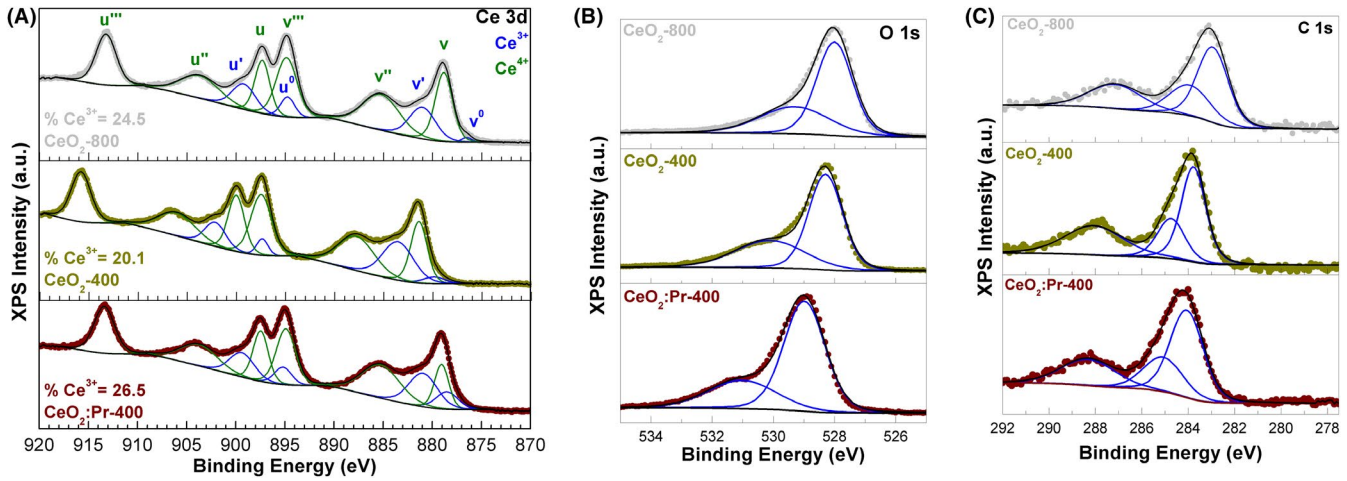

FIGURE 4 XPS spectra of (A) Ce 3d, (B) O 1s, and (C) C 1s photoemission forCeO_2-400, CeO_2-800 and CeO_2:Pr-400 samples [Color figure can be viewed at wileyonlinelibrary.com]

calculated and the values are 20.1%, 26.5%, and 24.6% for CeO_2-400, CeO_2:Pr-400, and CeO_2-800, respectively. Thus, Pr incorporation caused an increase in the amount of Ce^{3+} ions. In general, the doping with Pr is expected to result in the change Ce^{4+}/Ce^{3+},[42] and the same trend was observed in the $Ce_{1-x}Pr_xO_2$. Moreover this result can indicate a lower degree of Pr^{4+} formation, since the formation of Ce^{3+} becomes more difficult in the fluorite lattice with more quantity of Pr^{4+}.[42] It has been reported that Pr^{3+} instead of Ce^{4+} ions occur because the excess electrons from the reduction process tend to be located at the Pr^{4+} ions.[43]

Figure 4B shows the O 1s XPS spectra for CeO_2-400, CeO_2:Pr-400, and CeO_2-800. Two different O species with peaks centered around 528 eV and 530 eV were observed. The first one is characteristic of the lattice oxygen forming the fluorite structure with cerium, whereas the second one can be attributed to the oxygen bound to carbon components.[44] This result is in agreement with C 1s XPS spectrum, which is exhibited in Figure 4C. Three peaks can fit the C 1s spectra centered around 284, 285 and 288 eV, whose binding energies are related to C-C, C-O-C, and C = O-C, respectively.[45] Indeed, there is the formation of -Ce-OOC-C(OH)-COOH complexes in the synthesis of CeO_2 via the polymeric precursor method due the coordination of Ce^{4+} with citric acid. These complexes polymerize with the reaction between COOH groups and ethylene glycol (that contains a large amount of $-CH_2$ and -OH groups), resulting in the creation of a polymer resin of the type -Ce-OOC-C-COOC-$(CH_2)_n$-COO-Ce-.[31,32] Majority of this resin will decompose into H_2O and CO_2 during the pyrolysis procedure. These decomposition products are mostly removed from the system; however, residues can create defects in the forming CeO_2 lattice, such as interstitial or substitutional carbon. These organic species are linked to Ce-O-Ce networks, such as Ce-O-C-C-R, -Ce-O-C-O-Ce-, etc The Ce-O bond energy is lower than that of the C-O, whose values are approximately 790 and 1077 kJ/mol, respectively.[46]

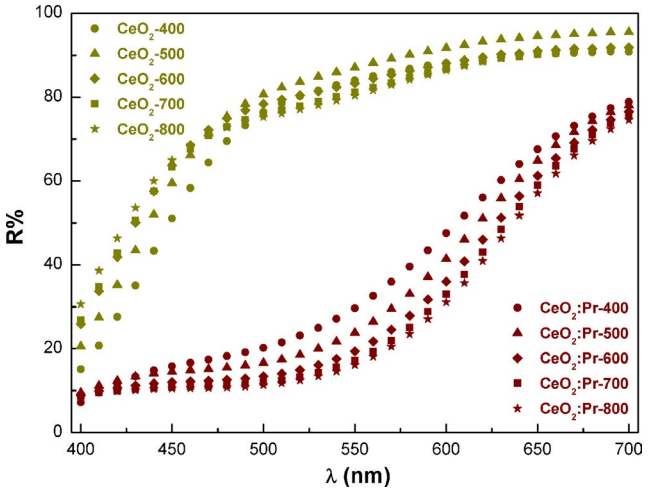

FIGURE 5 UV-vis reflectance spectra for CeO_2 and CeO_2:Pr samples as a function of the annealing temperature [Color figure can be viewed at wileyonlinelibrary.com]

The bond cleavage on chemical and thermal environment presents a significant dependence on the order of the bond energies.[31,32] Consequently, the initial cleavage occurs at the Ce-O bonds with subsequent annealing, which modifies the intermolecular chemical environment and removes a portion of the oxygen from the network along with the carbon.[31,32] Hence, an increase in the number of oxygen vacancies and Ce^{3+} ions would be caused by the increase of the annealing temperature as a consequence of the charge compensation, explaining the results of Raman and XPS analysis.

Figure 5 shows the UV-vis reflectance spectra for CeO_2 and CeO_2:Pr samples as a function of the annealing temperature. As can be seen, CeO_2 samples absorb blue light (400-450 nm), which originates from the O 2p Ce 4f charge-transfer transitions.[5] Because of the absorption in the blue region, a complementary light-yellow color is observed for these

samples.[5,7] As the annealing temperature increases, the reflectance spectra shift to lower wavelength, decreasing the absorption in the blue region. As a result, the samples show the tendency to become white. Through the reflectance spectra, the calculated band gap between the anionic band and the cationic band is 2.44 and 2.57 eV for CeO_2-400 and CeO_2-800 samples, respectively. This difference and the variation in the hue are associated with the oxygen vacancies promoted with the annealing, as shown in XPS and Raman measurements. When one O vacancy forms, two unpaired electrons localize on the two Ce^{4+} ions immediately surrounding the vacancy, resulting in two Ce^{3+} ions with f^1 configuration.[47]

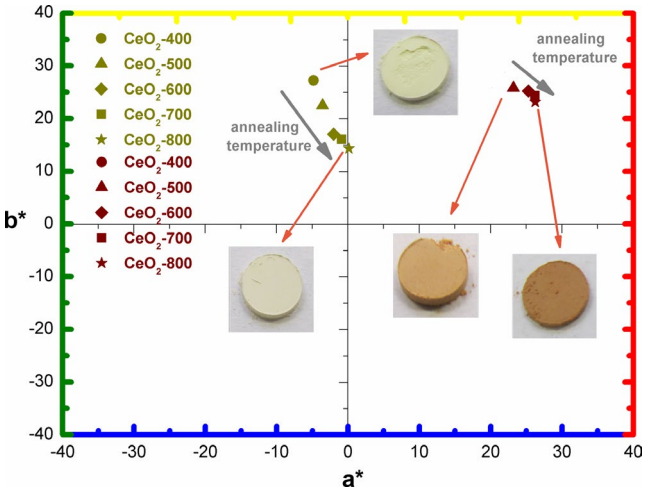

FIGURE 6 Colorimetric coordinates and photographs for CeO_2 and CeO_2:Pr samples as a function of the annealing temperature [Color figure can be viewed at wileyonlinelibrary.com]

The incorporation of Pr ions into CeO_2 matrix introduces an additional electronic level of energy between the O^{2-} valence band and Ce^{4+}conduction band by $4f^1$ electron of the praseodymium valence shell, which reduces the band gap.[4] The calculated band gap obtained through the reflectance spectra is 1.82 and 1.81 eV for CeO_2:Pr-400 and CeO_2:Pr-800, respectively. As can be seen in Figure 5, CeO_2:Pr samples present absorption in the region below 550 nm, producing a red color, in agreement with reports from the literature.[3,4,7,8,10,12] Masó et al obtained similar results for samples prepared by solid-state reaction with the same composition ($Ce_{0.990}Pr_{0.010}O_{2-\delta}$).[11] As the annealing temperature increases, the edge in the reflectance spectra shifts to higher wavelengths, resulting in the modification of the hue, from a red-orange color to a red-brown one. This behavior is associated with the formation of oxygen vacancies with the annealing, in which electrons left by charged oxygen vacancies preferentially localize on Pr atoms, and is consistent with the observed charge transfer spectra of lanthanide ions in oxides.[11,47]

The colorimetric coordinates (L*, a*, b*) of CeO_2 and CeO_2:Pr samples using D65-10 (daylight) light source according to the CIE-L*a*b* standard colorimetric method are exhibited in Figure 6. These colorimetric coordinates must be analyzed jointly to determine the final color of pigments, especially the a* and b* coordinates. Figure 6 shows also photographs of the as-prepared powders and samples annealed at 800°C. As discussed above, the CeO_2-400 sample has light-yellow color because of the absorption in the blue region. As the annealing temperature increases, the luminance parameter (L*) remains almost constant, whereas the red parameter (+a*) increases and the yellow parameter (+b*) decreases. These parameters as a function

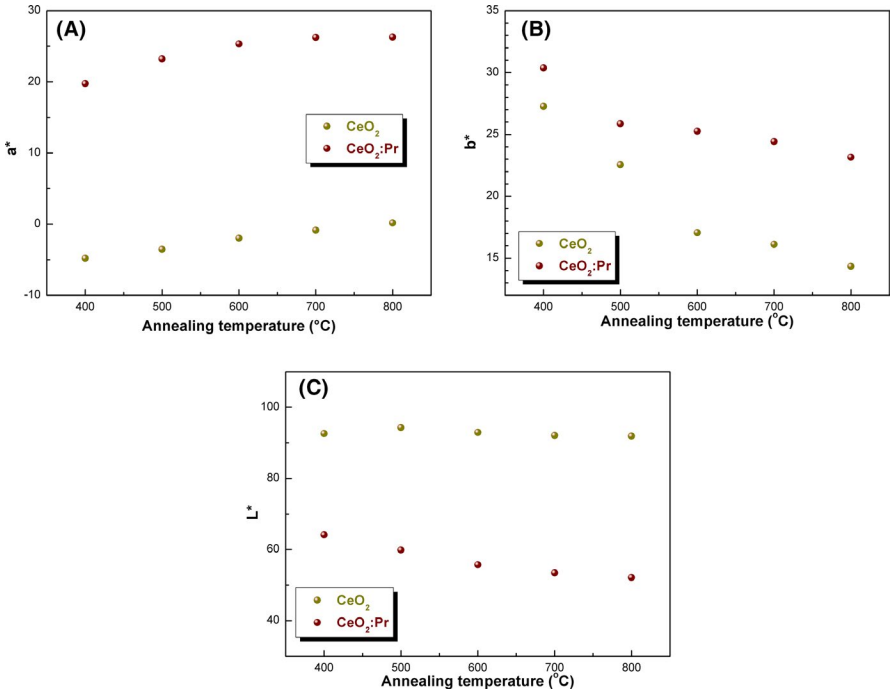

FIGURE 7 (A) a*, (B) b*, and (C) L* parameters as a function of the annealing temperature [Color figure can be viewed at wileyonlinelibrary.com]

of the annealing temperature are shown in Figure 7. As a result, the sample annealed at 800°C shows a white coloration with a total color difference (ΔE*) equals 13.75 compared to CeO_2-400 sample, which is considered very large.[48] With Pr-doping for the as-prepared sample, a red-orange coloration was observed. The L* and b* parameters decrease, whereas the a* parameter increases with the annealing temperature, resulting in a modification in the hue for red-brown. According to Masó et al, a* values for $Ce_{0.990}Pr_{0.010}O_{2-\delta}$ sample calcined at 1440 and 1500°C are 20.91 and 20.53, whereas L* values are 61.98 and 58.18, respectively.[11] In our study, a* parameter ranges from 19.75 to 26.28 as the annealing temperature increases, indicating more intense red color at lower calcination temperature compared to the result reported in the literature.[11] Moreover L* parameter ranges from 64.16 to 52.13, meaning greater intensity for as-prepared sample. Furthermore, according to Masó et al,[11] best red color for $Ce_{0.990}Pr_{0.010}O_2$ sample was obtained by increasing the calcination temperature and during firing. Through this process, loss of oxygen from the fluorite lattice can result in the creation of oxygen vacancies,[11] in agreement with our results. Comparing CeO_2:Pr-400 and CeO_2:Pr-800 samples, the ΔE* is equal to 13.5 (very large difference). Thus, the annealing shows a substantial influence on the color of the based-CeO_2 pigments prepared by the polymeric precursor method. As discussed, in this synthesis method, carbon can be retained in the lattice of the crystalline pigment, which is released with heat treatment, resulting in the formation of oxygen vacancies. The charge compensation or charge transfer is responsible for the modification of the hue of these pigments.

4 | CONCLUSIONS

In this paper, nanostructured CeO_2 and CeO_2:Pr samples were synthesized using the polymeric precursor method, and their structural and optical characterizations were performed. FE-SEM images revealed a regular morphology of CeO_2 nanoparticles and a uniform particle size ranging from 22 to 28 nm according to the annealing temperature. Pr-doping does not show an influence on particle size. XRD results show that CeO_2 and CeO_2:Pr samples crystallized completely without the presence of secondary phases, and the diffraction patterns correspond to the cubic fluorite structure with *Fm*3*m* space group. Raman spectra show the fluorite F_{2g} mode, confirming the XRD results. With Pr-doping and the annealing of the samples, two bands were observed between 550 and 600 cm^{-1} which are related to the defects in the fluorite structure associated with oxygen vacancies. XPS spectra revealed the presence of carbon even in the samples annealed at higher temperatures due to the synthesis method, which involves the formation of a precursor polymeric resin. Moreover these measurements exhibit an increase in the ratio of Ce^{3+} ions as a function of annealing temperature and Pr-doping. This increase is associated with the carbon removal from the lattice with annealing. This behavior causes a change in the hue of the powders as the annealing temperature increases. According to diffuse reflectance and colorimetric measurements, CeO_2 shows a light-yellow color due to the O 2p Ce 4f charge-transfer transitions whose b* parameter mainly decreases with annealing, becoming almost white. On the other hand, CeO_2:Pr sample exhibits a red-orange color because of the electronic transitions between $4f^2 \rightarrow 5d^1$ states of Pr^{3+}. With the annealing, L* and b* parameters decrease, resulting in a red-brown shade. The charge compensation or charge transfer is responsible for the modification of the hue of these pigments. We believe that our results lay ground for cheaper and less toxic pigments based on Pr-doped cerium oxides.

ACKNOWLEDGMENTS

The authors thank FAPESP (through project 2013/12993-4), CNPq and Capes funding agencies. The authors also thank Leandro X. Moreno (Unesp – IGCE) for Raman measurements. This research has been financially supported by the Ministry of Education, Youth and Sports of the Czech Republic under the project CEITEC 2020 (LQ1601). The authors also thank the CEITEC Nano Research Infrastructure supported by MEYS CR (LM2018110).

ORCID

Vinicius Tadeu Santana https://orcid.org/0000-0002-2258-6140
Alexandre Mesquita https://orcid.org/0000-0001-8524-0959

REFERENCES

1. Bae B, Tamura S, Imanaka N. Novel environment-friendly yellow pigments based on praseodymium(III) tungstate. Ceram Int. 2017;43(9):7366–8.
2. Jovaní M, Fortuño-Morte M, Beltrán-Mir H, Cordoncillo E. Environmental-friendly red-orange ceramic pigment based on Pr and Fe co-doped $Y_2Zr_2O_7$. J Eur Ceram Soc. 2018;38(4):2210–7.
3. Olegário RC, Souza ECF, Borges JFM, Cunha JBM, Andrade AVC, Antunes SRM, et al. Synthesis and characterization of Fe^{3+} doped cerium-praseodymium oxide pigments. Dye Pigments. 2013;97(1):113–7.
4. Kumari LS, Rao PP, Koshy P. Red pigments based on CeO_2-MO_2-Pr_6O_{11} (M=Zr and Sn): Solid solutions for the coloration of plastics. J Am Ceram Soc. 2010;93(5):1402–8.
5. Wendusu KD, Masui T, Imanaka N. Novel environmentally friendly inorganic yellow pigments based on CeO_2-SiO_2-Al_2O_3-Bi_2O_3. Bull Chem Soc Jpn. 2013;86(2):283–8.
6. Bernardi MIB, Mesquita A, Béron F, Pirota KR, Zevallos AO, Doriguetto AC, et al. The role of oxygen vacancies and their location in the magnetic properties of $Ce_{1-x}Cu_xO_{2-\delta}$ nanorods. Phys Chem Chem Phys. 2015;17(5):3072–80.
7. Kumari LS, Rao PP, Sameera S, Koshy P. Synthesis and optical properties of $Ce_{0.95}Pr_{0.05-x}M_xO_2$ (M = Mn, Si) as potential

ecological red pigments for coloration of plastics. Ceram Int. 2012;38(5):4009–16.
8. Sulcova P, Trojan M. Study of $Ce_{1-x}Pr_xO_2$ pigments. Thermochim Acta. 2003;395(1–2):251–5.
9. Aruna ST, Ghosh S, Patil KC. Combustion synthesis and properties of $Ce_{1-x}Pr_xO_{2-\delta}$ red ceramic pigments. Int J Inorg Mater. 2001;3(4–5):387–92.
10. Kumari LS, Rao PP, Reddy ML. Environment-friendly red pigments from CeO_2-Fe_2O_3-Pr_6O_{11} solid solutions. J Alloys Compd. 2008;461(1–2):509–15.
11. Masó N, Beltrán H, Muñoz R, Julián B, Carda JB, Escribano P, et al. Optimization of praseodymium-doped cerium pigment synthesis temperature. J Am Ceram Soc. 2003;86(3):425–30.
12. Olazcuaga R, Le Polles G, El Kira A, Le Flem G, Maestro P. Optical properties of $Ce_{1-x}Pr_xO_2$ powders and their applications to the coloring of ceramics. J Solid State Chem. 1987;71(2):570–3.
13. Titirici MM, Antonietti M, Thomas A. A generalized synthesis of metal oxide hollow spheres using a hydrothermal approach. Chem Mater. 2006;18(16):3808–12.
14. Cao CY, Cui ZM, Chen CQ, Song WG, Cai W. Ceria hollow nanospheres produced by a template-free microwave-assisted hydrothermal method for heavy metal ion removal and catalysis. J Phys Chem C. 2010;114(21):9865–70.
15. Dziembaj R, Molenda M, Chmielarz L, Drozdek M, Zaitz MM, Dudek B, et al. Nanostructured Cu-doped ceria obtained by reverse microemulsion method as catalysts for incineration of selected VOCs. Catal Letters. 2010;135(1–2):68–75.
16. Gamarra D, Munuera G, Hungría AB, Fernández-García M, Conesa JC, Midgley PA, et al. Structure-activity relationship in nanostructured copper-ceria-based preferential CO oxidation catalysts. J Phys Chem C. 2007;111(29):11026–38.
17. Gamarra D, Belver C, Fernández-García M, Martínez-Arias A. Selective CO oxidation in excess H2 over copper-ceria catalysts: Identification of active entities/species. J Am Chem Soc. 2007;129(40):12064–5.
18. Avgouropoulos G, Ioannides T, Matralis H. Influence of the preparation method on the performance of CuO–CeO_2 catalysts for the selective oxidation of CO. Appl Catal B Environ. 2005;56(1-2):87–93.
19. Farahmandjou M, Zarinkamar M, Firoozabadi TP. Synthesis of Cerium Oxide (CeO_2) nanoparticles using simple CO-precipitation method. Rev Mex Física. 2016;62:496–9.
20. Farahmandjou M, Dastpak M. Fe-Loaded CeO_2 nanosized prepared by simple co-precipitation route. Phys Chem Res. 2018;6(4):713–20.
21. Avgouropoulos G, Ioannides T. Selective CO oxidation over CuO-CeO_2 catalysts prepared via the urea-nitrate combustion method. Appl Catal A Gen. 2003;244(1):155–67.
22. Avgouropoulos G, Ioannides T, Papadopoulou C, Batista J, Hocevar S, Matralis HK. A comparative study of Pt/γ-Al_2O_3, Au/α-Fe_2O_3 and CuO-CeO_2 catalysts for the selective oxidation of carbon monoxide in excess hydrogen. Catal Today. 2002;75(1–4):157–67.
23. Dastpak M, Farahmandjou M, Firoozabadi T. Synthesis and preparation of magnetic Fe-Doped CeO_2 nanoparticles prepared by simple Sol-Gel method. J Supercond Nov Magn. 2016;29:2925–9.
24. Pechini MP. inventor; Sprague Electric Co, assignee. Method of Preparing Lead and Alkaline Earth Titanates and niobates and coating method using the same to form a capacitor. United States patent US3330697A. 1967 Jul 11.
25. Kakihana M. "Sol-Gel" preparation of high temperature superconducting oxides. J Sol-Gel Sci Technol. 1996;6(1):7–55.
26. Rana N, Chand S, Gathania AK. Band gap engineering of ZnO by doping with Mg. Phys Scr. 2015;90(8):85502.
27. Carvalho KTG, Fidelis SC, Lopes OF, Ribeiro C. Effect of processing variables on the photocatalytic properties of ZnO thin films prepared using the polymeric precursor method. Ceram Int. 2015;41(9):10587–94.
28. Rana N, Chand S, Gathania AK. Tailoring the structural and optical properties of ZnO by doping with Cd. Ceram Int. 2015;41(9):12032–7.
29. Potemkin DI, Snytnikov PV, Pakharukova VP, Semin GL, Moroz EM, Sobyanin VA. Copper-cerium oxide catalysts prepared by the Pechini method for CO removal from hydrogen-containing mixtures. Kinet Catal. 2010;51(1):119–25.
30. Araújo VD, Bernardi MIB. Synthesis and optical and structural characterization of $Ce_{(1-x)}O_2$:M_xO (M = Cu, Co) pigments. J Therm Anal Calorim. 2011;103(2):501–6.
31. Lin C, Zhang C, Lin J. Phase transformation and photoluminescence properties of nanocrystalline ZrO_2 powders prepared via the pechini-type sol-gel process. J Phys Chem C. 2007;111(8):3300–7.
32. Cury de Oliveira R, Martins DE, Basso Bernardi MI, Mesquita A. $Zn_{1-x}Mg_xO$ nanoparticles prepared by the polymeric precursor method: Correlation between photoluminescence and local structure. Opt Mater (Amst). 2018;86:71–8.
33. Shirley DA. High-resolution x-ray photoemission spectrum of the valence bands of gold. Phys Rev B. 1972;5(12):4709–14.
34. International Commission on Illumination. Recommendations of uniform color spaces, color difference equations, phychometrics color terms. CIE Publication. 1978;1(15).
35. Mesquita A, Bernardi MIB, Godart C, Pizani PS, Michalowicz A, Mastelaro VR. Grain size effect on the structural and dielectric properties of $Pb_{0.85}La_{0.15}TiO_3$ ferroelectric ceramic compound. Ceram Int. 2012;38(7):5879–87.
36. Shannon RD. Revised effective ionic radii and systematic studies of interatomic distances in halides and chalcogenides. Acta Crystallogr Sect A. 1976;32(5):751–67.
37. Klug MP, Alexander LE. X-ray diffraction procedure for polycrystalline and amorphous materials. New York, NY: Wiley-Interscience Publication; 1974.
38. Chattopadhyay S, Ayyub P, Palkar VR, Multani M. Size-induced diffuse phase transition in the nanocrystalline ferroelectric $PbTiO_3$. Phys Rev B. 1995;52(18):13177–83.
39. Li L, Chen F, Lu JQ, Luo MF. Study of defect sites in $Ce_{1-x}M_xO_{2-\delta}$ (x = 0.2) solid solutions using raman spectroscopy. J Phys Chem A. 2011;115(27):7972–7.
40. Sohn H, Celik G, Gunduz S, Dogu D, Zhang S, Shan J, et al. Oxygen mobility in pre-reduced nano- and macro-ceria with Co loading: An AP-XPS, In-Situ DRIFTS and TPR Study. Catal Letters. 2017;147(11):2863–76.
41. Vovchok D, Guild CJ, Dissanayake S, Llorca J, Stavitski E, Liu Z, et al. In situ characterization of mesoporous Co/CeO_2 catalysts for the high-temperature water-gas shift. J Phys Chem C. 2018;122(16):8998–9008.
42. Zoellner MH, Niu G, Jhang JH, Schaefer A, Zaumseil P, Bäumer M, et al. Temperature-dependent reduction of epitaxial $Ce_{1-x}Pr_xO_{2-\delta}$ (x = 0–1) thin films on Si(111): A combined temperature-programmed desorption, X-ray diffraction, X-ray photoelectron spectroscopy, and raman study. J Phys Chem C. 2013;117(47):24851–7.

43. Tang Y, Zhang H, Cui L, Ouyang C, Shi S, Tang W, et al. First-principles investigation on redox properties of M-doped CeO2 (M=Mn, Pr, Sn, Zr). Phys Rev B - Condens Matter Mater Phys. 2010;82(12):125104.
44. Amadine O, Essamlali Y, Fihri A, Larzek M, Zahouily M. Effect of calcination temperature on the structure and catalytic performance of copper-ceria mixed oxide catalysts in phenol hydroxylation. RSC Adv. 2017;7(21):12586–97.
45. Trino LD, Dias LFG, Albano LGS, Bronze-Uhle ES, Rangel EC, Graeff CFO, et al. Zinc oxide surface functionalization and related effects on corrosion resistance of titanium implants. Ceram Int. 2018;44(4):4000–8.
46. Lide DR. CRC handbook of chemistry and physics, 84th edn. Boca Raton: CRC Press; 2003.
47. Niu G, Schubert MA, D'Acapito F, Zoellner MH, Schroeder T, Boscherini F. On the local electronic and atomic structure of $Ce_{1-x}Pr_xO_{2-\delta}$ epitaxial films on Si. J Appl Phys. 2014;116(12):123515.
48. Lima NA, Alencar LDS, Siu-Li M, Feitosa CAC, Mesquita A, M'peko JC, et al. $NiWO_4$ powders prepared via polymeric precursor method for application as ceramic luminescent pigments. J Adv Ceram. 2020;9(1):55–63.

How to cite this article: Gonzaga LA, Santana VT, Bernardi MIB, Hrubý J, Neugebauer P, Mesquita A. CeO_2 and CeO_2:Pr nanocrystalline powders prepared by the polymeric precursor method: Yellow and red pigments with tunable color. *J Am Ceram Soc*. 2020;103:6280–6288. https://doi.org/10.1111/jace.17339